Feasibility of an optical fiber clock

Ekaterina Ilinova,[1] James F. Babb,[2] and Andrei Derevianko[1]
[1]*Department of Physics, University of Nevada, Reno, Nevada 89557, USA*
[2]*Harvard-Smithsonian Center for Astrophysics, 60 Garden Street, MS 14, Cambridge, Massachusetts 02138, USA*
(Received 16 May 2017; published 8 September 2017)

We explore the feasibility of a fiber clock, i.e., a compact, high-precision, optical lattice atomic clock based on atoms trapped inside a hollow-core optical fiber. Such a setup offers an intriguing potential both for a substantially increased number of interrogated atoms (and thereby an improved clock stability) and for miniaturization. We evaluate the sensitivity of the $^1S_0$-$^3P_0$ clock transition in Hg and other divalent atoms to the fiber inner core surface at nonzero temperatures. The Casimir-Polder interaction induced $^1S_0$-$^3P_0$ transition frequency shift is calculated for the atom inside the hollow capillary as a function of atomic position, capillary material, and geometric parameters. For Hg atoms on the axis of a silica capillary with inner radius $\geqslant 15\,\mu$m and optimally chosen thickness $d \sim 1\,\mu$m, the atom-surface interaction induced $^1S_0$-$^3P_0$ clock transition frequency shift can be kept on the level $\delta\nu/\nu_{\rm Hg} \sim 10^{-19}$. We also estimate the atom loss and heating due to collisions with the buffer gas, lattice intensity noise induced heating, spontaneous photon scattering heating, and residual birefringence induced frequency shifts.

DOI: 10.1103/PhysRevA.96.033814

I. INTRODUCTION

The rapid progress in micro- and nanofabrication technologies and advances in material science together with the growing demand for precision metrology and quantum information processing gave rise to a new branch of research engineering aiming to develop miniaturized quantum devices. Examples include atomic clocks [1–4], atomic sensors, interferometers [5–9], and quantum logic gates [10]. In particular, development of miniaturized atomic clocks is anticipated to enable important applications requiring portability and low power consumption, such as secure telecommunications [11,12], mobile timing, navigation [13–15], and deep space atomic clocks [16].

The main platforms for compact quantum devices are microelectromechanical systems [17,18], miniaturized wire traps [19], and, more recently, hollow-core optical fibers [20,21]. Here we analyze the feasibility of a "fiber clock"—a device that holds interrogated clock atoms inside a hollow-core optical fiber. The atoms are optically trapped, avoiding collisions with the wall surface [21]. The fiber clock is a natural extension of optical lattice clocks [22], which recently reached record levels of estimated fractional inaccuracy at the $\approx 6 \times 10^{-18}$ level [23,24]. The clock transition is the narrow $^1S_0$-$^3P_0$ transition present in divalent atoms (e.g., Sr, Yb, Ca, Mg, and Hg). Unlike in the free space configuration, where the maximum interaction length does not exceed the Rayleigh length $z_R = \pi w_0^2/\lambda$ (here w_0 is the characteristic Gaussian beam waist radius and λ is the wavelength of the laser field), the fiber clock setup does not suffer from this limitation [21]. Large ensembles of cold atoms trapped in a one-dimensional (1D) optical lattice can be realized within the compact transverse region $\sim$5-100μm, avoiding high atomic density per lattice site. The increase in the number of interrogated atoms enables further advances in clock stability. Improved stability, i.e., the ability to average down statistical noise in shorter time intervals, is beneficial in many applications. In particular, searches for short transient variation of fundamental constants induced by "clumpy" dark matter [25,26] would benefit from the improved clock stability.

In pursuing a superprecise miniature clock one also needs to keep in mind the miniaturization of other clock elements. In this context, it is important to note that the fiber clock can be integrated into the all-fiber framework. Moreover, one could envision the enhanced superradiance [27] of the 1D trapped atomic ensemble into the fiber guided laser mode. Optical trapping of large ensembles of cold divalent atoms uniformly distributed over the length $L \sim N_a\lambda_{\rm L}/2$ (where $N_a \gg 1$ is the number of trapped atoms and $\lambda_{\rm L}$ is the lattice wavelength) inside the hollow-core fiber and suppressing the associated sources of atomic dipole relaxation (other than the radiative decay) will be the next step toward an ultranarrow-linewidth laser source at the $^1S_0$-$^3P_0$ clock transition frequency. Superradiant lasing on the clock transition [28,29] is a potential alternative to space-consuming bulky reference cavities used in optical clocks.

Here we theoretically evaluate the feasibility of the optical lattice clock based on the narrow $^1S_0$-$^3P_0$ transition in Hg and other alkaline-earth-metal-like atoms (Cd, Mg, Yb, Sr) optically trapped inside a hollow-core fiber. One of the first experimental efforts toward compact optical clocks involved the 3D trapping of an ensemble of Sr atoms inside a micron-sized structure [18]. More recently, a precision spectroscopy of the $^1S_0$-$^3P_1$ transition of Sr atoms optically trapped inside a kagome fiber has been demonstrated [21]. To the best of our knowledge, no $^1S_0$-$^3P_0$ transition based optical lattice clock has been realized so far with cold atoms inside a hollow-core fiber. A mercury clock [30–34] is of particular interest in applications to probing physics beyond the standard model due to the large value of the Hg nuclear charge. The relatively low static polarizability of Hg and Cd [30] makes them less sensitive to black-body radiation (BBR), as compared to Sr, Yb, and Ca. This peculiarity makes Hg and Cd good candidates for optical clock applications where the ambient temperature is difficult to control, making the BBR shift the main constraint on the clock accuracy [35].

As a platform for the Hg and Cd clocks, one could consider recently developed UV guiding hollow-core fibers [36,37]. In [37], a single-mode photonic crystal fiber with inner core diameter $\approx$20 μm and loss $\approx$0.8 dB/m at the wavelength

280 nm was demonstrated. In [36], a multimode hollow-core fiber with the inner core diameter ≈25 μm and loss ≈2 dB/m at wavelength 355 nm and a loss of ≈0.4 dB/m at the wavelength 250 nm was designed. The ability to design similar waveguides for the UV range has been announced [36].

The development of a fiber-based atomic clock requires detailed understanding of the effects of the surrounding surface on the clock transition frequency. The previous evaluation of the surface-induced clock frequency shifts for divalent atoms was carried out for planar geometry [38]. Here we take into account the cylindrical fiber geometry and its material properties. The atom-surface interaction generally depends on the geometry and the fiber material. In [39], the Casimir-Polder (CP) interaction of Rydberg atoms with a cylindrical cavity was analyzed. It was shown that at certain cavity radii an enhancement of modes resonant with atomic transitions may occur, leading to an increase of the resonant part of CP interaction potential and to the modification of the atomic radiative decay rate [39,40].

Considering the high precision required for the optical clock, we study these resonant effects for the ground $^1S_0$ and the metastable $^3P_0$ clock states of alkaline-earth-metal-like atoms. We present the general form of the long-range atom-surface interaction potential at nonzero temperatures for the hollow-core cylindrical geometry and analyze the resulting $^1S_0$-$^3P_0$ clock frequency shift as a function of the fiber parameters. We find that for an ensemble of Hg atoms optically trapped near the axis of a hollow silica capillary waveguide with inner radius $R_{\rm in} \geqslant 15$ μm, the CP interaction-induced fractional frequency shift can be suppressed down to the level of $\delta\nu/\nu \sim 10^{-19}$. The frequency shift due to the nonresonant part of the CP interaction in this case is dominant compared to the resonant contribution. For the atoms trapped near the capillary axis, the CP interaction decreases with the growth of the inner core radius. At high relative permittivity of the inner core surface material $\varepsilon_r \gg 1$ the contribution of resonant atom-surface interaction as well as the radiative decay rate enhancement (Purcell effect) may become dominant at certain choices of the geometric parameters of the waveguide. Both the clock transition frequency shift caused by the resonant part of CP interaction potential and the Purcell effect can be suppressed by slightly adjusting the thickness d at a given inner core radius $R_{\rm in}$. The adjustment has to be done in order to avoid the resonant waveguide modes at the frequencies of the decay channels. For more complex waveguide geometries the resonances of the atom-surface interaction as a function of the waveguide parameters can be more difficult to predict.

The paper is organized as follows: In Sec. II we evaluate the CP-induced clock frequency shifts and in Sec. III we consider other effects, such as the atomic loss and heating inside the fiber. The summary is given in Sec. IV. In Secs. II and III, theoretical expressions are given in Gaussian units, while in Sec. IV, we also use atomic units, as indicated.

II. $^1S_0$-$^3P_0$ CLOCK TRANSITION INSIDE THE HOLLOW-CORE FIBER

The probability of BBR induced transitions from the clock levels to the other atomic states is negligibly small over the typical clock operation time and the clock atoms are not in thermal equilibrium with the BBR bath [41]. The CP interaction induced shift of the clock frequency has to be found as the difference of free energy shifts of the clock levels [39,41]:

$$\delta F_a(\mathbf{r}) = \frac{4\pi}{3}\sum_j \{n(|\omega_{ja}|) - \Theta(\omega_{aj})[1+2n(|\omega_{aj}|)]\}|\mu_{aj}|^2 \times \mathrm{Tr}[\mathrm{Re}\mathbf{G}(\mathbf{r},\mathbf{r},|\omega_{ja}|)] - k_B T \sum_{k=0}^{\infty\,\prime} \mathrm{Tr}[\mathbf{G}(\mathbf{r},\mathbf{r},i\xi_k)]\alpha_a(i\xi_k), \quad (1)$$

where $\xi_k = 2\pi k_B T k/h$ is the kth Matsubara frequency, T is the temperature, μ_{aj} is the dipole matrix element of transition $a \to j$ with transition frequency ω_{ja}, $\mathbf{G}(\mathbf{r},\mathbf{r},\omega)$ is the classical Green's tensor [42–44] for a given waveguide geometry, α_a is the atomic polarizability, the prime on the Matsubara sum indicates that the $k = 0$ term is to be taken with half weight, and Θ is the Heaviside step function. We do not present the details of the full theoretical framework used in these calculations as it was previously done by other authors, see Refs. [39,41] and references therein.[1] We approximate the geometry of the

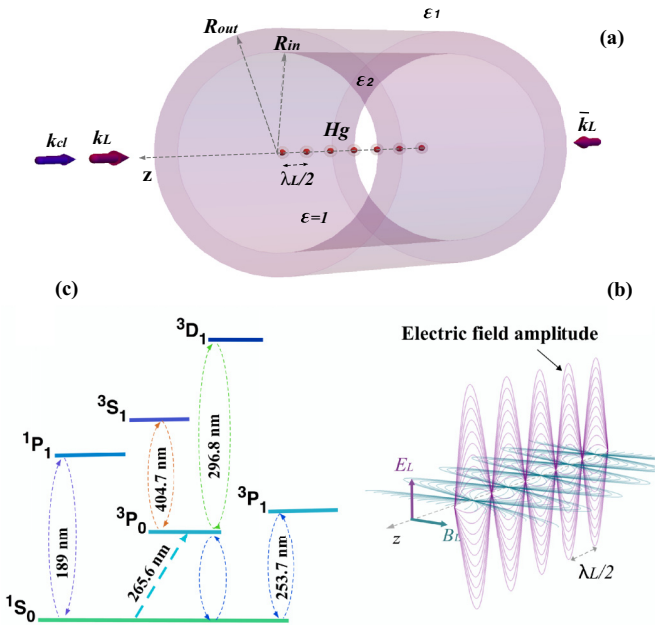

FIG. 1. (a) Cold atoms optically trapped in the ground vibrational state inside the hollow-core dielectric cylinder. (b) Energy level diagram for Hg atoms: the clock transition is shown with the dashed straight arrow, and dashed lines show the virtual transitions contributing to the resonant part of the Casimir-Polder interaction potential. (c) Schematic representation of the optical lattice field spatial distribution.

[1]The factor $\xi_j^2/(c^2\epsilon_0)$ in Eq. (2.3) and the factor $\mu_0\omega_{kn}^2$ in Eq. (2.7) of Ref. [39] are included through the factor ω^2/c^2, expressed in Gaussian units, appearing in our expression for Green's tensor, see Eq. (2) below, and accounts for the factor 4π in our Eq. (1).

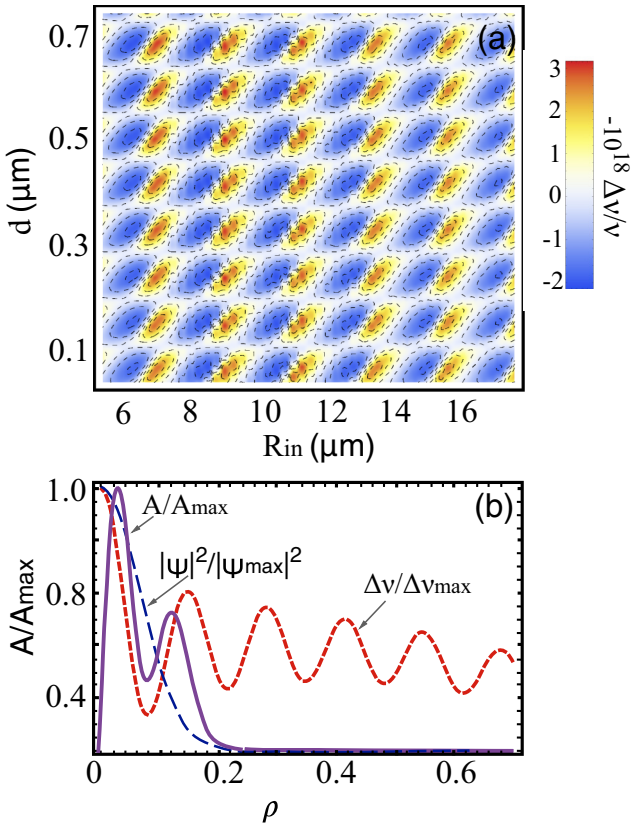

FIG. 2. (a) ^{199}Hg $^1S_0$-$^3P_0$ clock transition frequency shift due to the resonant part of the atomic interaction with the inner surface of a silica capillary as a function of its thickness d and inner radius $R_{\rm in}$ on the capillary axis $\rho = 0$. The rate of the $^1S_0$-$^3P_0$ transition $\gamma_{^1S_0\text{-}^3P_0} = 0.6\ {\rm s}^{-1}$ from [34] was used in our calculations. (b) The normalized value of $A = \rho\Delta\nu(\rho)|\psi(\rho)|^2$ (purple solid line) as a function of atom position ρ inside the capillary at the inner core radius $R_{\rm in} = 15\ \mu$m and the thickness $d = 1\ \mu$m. The short dashed red and blue dashed curves show the normalized values of the frequency shift $\Delta\nu/\Delta\nu_{\rm max}$ and the amplitude of the ground vibrational state wave function for the atom inside the red detuned optical lattice with trapping potential depth $U = 180\ \mu$K.

fiber inner interface as that of a cylindrical dielectric capillary of a given thickness $d = R_{\rm out} - R_{\rm in}$, see Fig. 1(a), where $R_{\rm in}$ and $R_{\rm out}$ are the inner and outer radii of the capillary and ρ is the radial coordinate of the atom inside the cylinder. We consider the surface to be in thermal equilibrium with the BBR at given temperature $T = T_S$. The mean occupation number n of photons with energy $\hbar\omega_{ja}$ is given by the Bose-Einstein distribution, $n(\omega_{ja}) = (e^{\hbar\omega_{ja}/k_BT_S} - 1)^{-1}$. Cold atoms prepared in a given state (either $^1S_0$ or $^3P_0$) are trapped by the red-detuned standing wave forming the 1D optical lattice inside the fiber, see Fig. 1. The "magic" wavelength of the laser field forming the lattice is chosen in order to cancel the differential ac Stark shift for the clock transition, $\lambda_L = 360$ nm [30]. The atomic ensemble temperature can be reduced down to a few nK [30], decreasing the trapping potential depth to $U \sim 10E_R$, where E_R is the recoil energy. We also assume that the atoms are trapped in the ground vibrational motional state and are located near the lattice nodes, corresponding to the maxima of the lattice field intensity, along the axis of a cylinder ($\rho = 0$), where they are most distant from the dielectric walls.

A. Resonant atom-surface interaction

We start our analysis of the $^1S_0$-$^3P_0$ clock transition frequency shift with the first term in Eq. (1), corresponding to the virtual dipole absorption and emission of thermal photons. In the presence of surface polaritons [41] or waveguide modes at the atomic transitions frequencies ω_{ja} these terms may become resonant [39]. The dashed lines in Fig. 1(b) indicate the virtual transitions contributing to the resonant part of the CP interaction potential. The term arising from the virtual emission $^3P_0 \rightsquigarrow {}^1S_0$ remains finite even at zero temperature, although it is strongly suppressed due to the small values of the corresponding dipole matrix elements for nonzero nuclear spin isotopes (these vanish for the nuclear spin-zero isotopes). Other contributions come from the virtual absorption of thermal photons via the $^3P_0$-$^3S_1$, $^3P_0$-$^3D_1$, $^1S_0$-$^1P_1$, and $^1S_0$-$^3P_{1,0}$ pathways. Their amplitudes are suppressed exponentially with decreasing surface temperature.

Figure 2 shows our computed fractional frequency shift of the $^1S_0$-$^3P_0$ clock transition for atoms on the capillary axis ($\rho = 0$) caused by the resonant part of the CP interaction potential at the surface temperature $T_S = 293$ K. One can see the resonant structure in its dependence on the capillary thickness parameter d and the inner radius $R_{\rm in}$. The effect ceases (on the capillary axis) as the capillary inner radii grow. For the vacuum-silica-air interface [45] the cavity effect is small compared to the case of highly reflective capillary material, Fig. 3. Also, there are no resonances in the relative permittivity $\varepsilon_{\rm silica}$ corresponding to transitions from the $^1S_0$ or $^3P_0$ clock states in divalent atoms. The upper limit on the resonant CP interaction induced clock transition frequency shift for Hg atoms on the capillary axis ($\rho = 0$) at surface temperature $T_S = 293$ K and inner core radius $R_{\rm in} = 15\ \mu$m is $|\delta\nu/\nu_{\rm Hg}| \sim 3 \times 10^{-18}$. It can be reduced further by choosing the optimal values of waveguide inner radius and thickness. For ^{87}Sr atoms the rate of the $^3\rho_0$-$^1S_0$ transition, contributing the most to the resonant CP interaction at the room temperature of the surface, is much lower than for ^{199}Hg. Therefore we do not

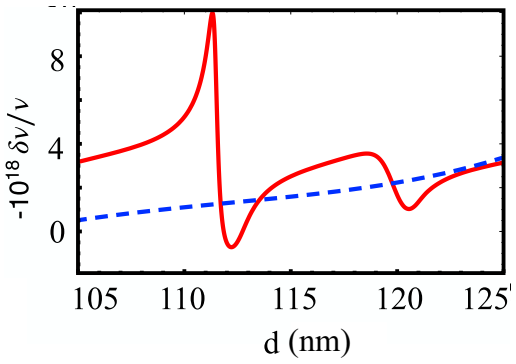

FIG. 3. ^{199}Hg $^1S_0$-$^3P_0$ clock transition frequency shift due to the resonant part of the atomic interaction with the inner surface of a silica capillary as a function of its thickness d at the fixed value of the inner radius $R_{\rm in} = 15.5\ \mu$m. The atoms are on the capillary axis $\rho = 0$, at two different values of relative permittivity of capillary material: $\epsilon_r = 2.45$ (blue dashed) and $\epsilon_r = 89$ (red solid).

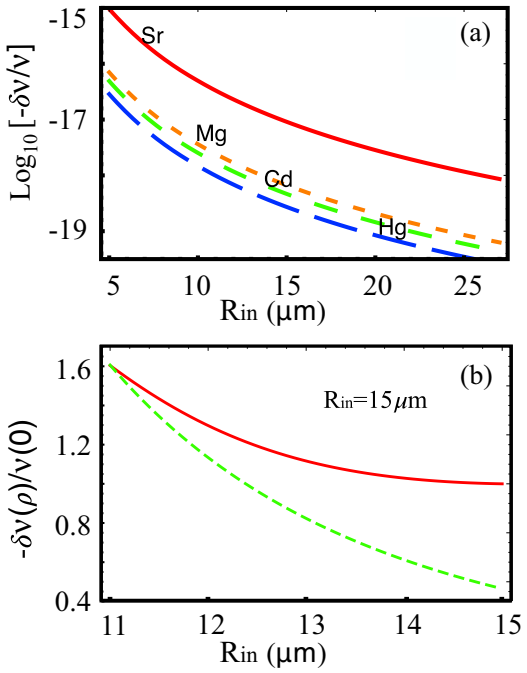

FIG. 4. (a) Frequency shift of the $^1S_0$-$^3P_0$ clock transitions in Hg (blue long-dashed), Cd (green medium-dashed), Mg (orange short-dashed), and in Sr (red solid) atoms due to the (dominant) nonresonant part of the Casimir-Polder interaction potential. The clock atoms are assumed to be located on the capillary axis. The capillary of thickness $d = 1$ μm has temperature $T_S = 77$ K. (b) Frequency shift of the $^1S_0$-$^3P_0$ clock transition in Hg atoms as a function of the distance $R_{\rm in} - \rho$ between the atom and the capillary inner surface. The capillary has the same parameters as in (a) with the fixed inner radius $R_{\rm in} = 15$ μm. The green dashed line shows the value $\delta\nu(\rho = 11\mu{\rm m})(\frac{11\mu{\rm m}}{R_{\rm in}-\rho})^4$ expected for CP interaction in the planar geometry.

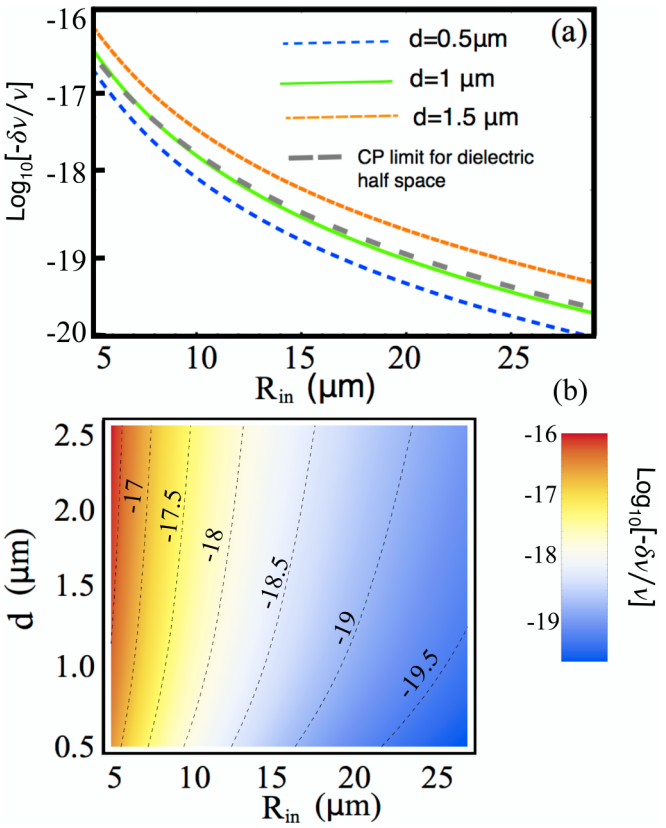

FIG. 5. (a) Frequency shift of the $^1S_0$-$^3P_0$ transition in Hg atoms originating from the nonresonant part of the CP interaction potential, as a function of the capillary inner radius $R_{\rm in}$ at different values of its thickness d. The gray dashed line shows the CP interaction limit for the dielectric half-space interface. (b) Dependence of the $^1S_0$-$^3P_0$ transition frequency shift (nonresonant part) in the Hg atom on the waveguide inner radius $R_{\rm in}$ and thickness d.

consider here the resonant CP interaction induced frequency shifts in the Sr atom.

The dependence of the resonant CP interaction on the waveguide geometry can be derived from the Green's function, given by [44]

$$\begin{aligned}&{\rm Tr}[{\rm Re}\mathbf{G}(\mathbf{r},\mathbf{r},\omega)]\\ &= \frac{i\omega^2}{2\pi c^2}\int_0^\infty dq \sum_{m=0}^{\infty\,\prime}\left\{\left(r_M + r_N\frac{q^2}{k^2}\right)\right.\\ &\left.\times\left[\frac{m^2}{\eta^2\rho^2}J_m^2(\eta\rho) + J_m'^{\,2}(\eta\rho)\right] + r_N\frac{\eta^2}{k^2}J_m^2(\eta\rho)\right\}, \qquad (2)\end{aligned}$$

where $r_{M,N}(m,q)$ are functions of the frequency ω and the surface parameters: $R_{\rm in}$, d, and ε, $\eta = \sqrt{k^2 - q^2}$, k is the wave vector, and J_m are the Bessel functions. The resonances in the $r_{M,N}$ coefficients at $q = 0$ determine the true resonances of the Green's function. On the axis $\rho = 0$ the resonant waveguide mode at the given frequency ω can be suppressed when minimizing the corresponding sum ${\rm Im}[r_N(0,0) + r_M(1,0)/2]$.

B. Nonresonant Casimir-Polder interaction potential

The second term in Eq. (1) corresponds to nonresonant quantum fluctuations of the atomic dipole. Away from resonances and at low surface temperatures this term is the primary contributor to the $^1S_0$ - $^3P_0$ transition frequency shift in divalent atoms.

Figure 4(a) shows the calculated clock transition frequency shift for the Hg, Cd, Mg, and Sr atoms on the silica capillary axis ($\rho = 0$) at surface temperature $T_S = 77$ K. In evaluating the shifts we used the dynamic electric polarizabilities from Refs. [38,46,47]. The Hg atom is least sensitive to the nonresonant atom surface interaction due to its relatively low differential static polarizability $\delta\alpha = \alpha_{^3P_0} - \alpha_{^1S_0}$ compared to the other divalent atoms (see Ref. [38] for extensive discussion of this point).

Figure 4(b) shows the calculated CP induced clock transition frequency shift for Hg as a function of the distance $R_{\rm in} - \rho$ between the atom and waveguide surface at the fixed value of the inner waveguide radius $R_{\rm in} = 15$ μm. ρ is the atomic position in cylindrical coordinates with the $\hat{z}$ axis placed at the waveguide symmetry axis. For a finite-size distribution of atomic motional wave function over the radial trapping

potential, this dependance will lead to broadening of the clock transition line.

Figure 5(a) illustrates the Hg $^1S_0$-$^3P_0$ transition frequency shift as a function of capillary inner radius at different values of the thickness parameter d. The gray dashed line shows the CP frequency shift for an atom interacting with the plane dielectric interface at the distance $z = R_{\rm in}$, $\delta\nu_{ab}^{\rm CP}(z) = -(3/8\pi)c\alpha_{ab}(0)z^{-4}$ [48], where $\alpha_{ab}(0)$ is the differential static polarizability of the atomic levels a and b. As the thickness of the capillary grows, the atoms on the axis are subject to stronger perturbation of their energy levels compared to the case of an atom near the flat dielectric interface. So, for example, at the thickness $d = 0.5$ μm and the inner radius 15 μm the atomic transition frequency shift is about 2.17 times smaller than the corresponding value for the flat interface. At the same inner radius value but increased thickness $d = 2.5$ μm, the atomic transition frequency shift is about 1.92 times larger than for the flat interface. As a comparison, in [49] the electrostatic approach was used to determine the van der Waals interaction of the atom with the inner surface of dielectric cylinder ($d \to \infty$). The interaction potential, as a function of the atom distance x from the surface, was parametrized there as $U(x) = -\varphi C_3/x^3$, with the factor $\varphi(\rho)$ depending on the distance ρ of the atom from the center of a cylinder. It was found that on the axis of a cylinder the interaction potential felt by the atom is 4 times stronger [$\varphi(0) = 4$] than for the atom near the dielectric plane surface at the distance equal to the cylinder radii.

Figure 5(b) shows the nonresonant CP interaction induced $^1S_0$-$^3P_0$ clock transition frequency shift in ^{199}Hg atoms as a function of the capillary inner radius and its thickness. One can see the steady frequency shift growth (absolute value) when increasing the capillary thickness and reducing the inner radius of the waveguide.

III. LIFETIME OF TRAPPED ATOMS AND OTHER SYSTEMATIC EFFECTS

In this section, we discuss the systematic effects limiting the lifetime of atoms in the optical lattice formed inside the fiber and, therefore, the stability of the fiber clock. We also compare various frequency shifts for the ^{199}Hg atom, which is the main focus of this paper, with those for the Sr, used in the most accurate to date optical lattice clock [23].

One of the detrimental effects comes from the atomic collisions with the residual buffer gas molecules. Compared to the macroscopic vacuum chamber, achieving high vacuum in the hollow-core fiber is more challenging due to the smallness of the inner core. Collisions of cold atoms with the background gas molecules inside the fiber lead to their heating and eventual escape from the trapping lattice. Considering that the average kinetic energy of the incident buffer gas molecule $E_{\rm bg}$ is much larger than that of the trapped atoms and that the scattering process (inside the shallow optical lattice) happens at relatively large internuclear distances R [so that $|V_{\rm col}(R) = -C_6/R^6| \ll E_{\rm bg}$, where C_6 is the van der Waals coefficient], one can consider the energy exchange between the two particles using the impulse approximation [50]. The resulting loss rate is given by $\gamma_{\rm loss} \approx \sqrt{\pi}n(\frac{2k_BT_b}{M})^{1/3}(\frac{15\pi C_6}{8\sqrt{2}mU})^{1/3}\Gamma(\frac{11}{6})$, where n is the buffer gas number density, M and m are, respectively, the masses of the buffer gas molecule and trapped atom, U is the trapping potential depth, and T_b is the temperature of the buffer gas. Here we assumed that $(1+\frac{m}{M})^2\frac{U}{2k_BT} \ll 1$. The residual buffer gas pressure in the experiments with cold atoms inside the hollow-core fiber [21,51] is $P_{\rm bg} \sim 10^{-6}$ Pa. The collisions of cold Hg atoms with molecular nitrogen N_2 at buffer gas pressure $P_{N_2} = 10^{-6}$ Pa, temperature $T_{N_2} = 293$ K and trapping potential depth $U = 10$ ER, Hg $= 3.67$ μK results in a Hg loss rate $\gamma_{\rm loss} = 0.37$ s^{-1}. This translates to almost half of the atoms escaping the optical lattice trap over 1 s. In our calculations, we used the van der Waals interaction constants C_6 given in [52]. The atom loss limits the interrogation time of the atomic ensemble $\tau_{\rm int} \sim 1/\gamma_{\rm loss}$ and the maximum number of atoms which can be loaded into the optical lattice inside the waveguide. Stronger lattice field intensities can be used during the guiding of the atoms along the fiber. After the atoms are distributed over the fiber length they can be decelerated and cooled further. The intensity of the lattice field then can be reduced. Lower residual gas pressure is required for further improvement of the clock effective operational time and accuracy. After interrogating the atomic ensemble over the time $\tau \sim 1/\gamma_{\rm loss}$, the lost atoms need to be evacuated from the fiber and the loading process repeated. The residual buffer gas density inside the fiber can be further reduced using light induced desorption [53] together with ultrahigh vacuum pumping techniques.

The collisional heating of the trapped atoms can be estimated as $\frac{dT_{\rm Hg}}{dt} = \frac{4\pi mM^2n}{(m+M)^2k_B}\langle v_r^3\int_0^{\chi_{\rm min}}\sigma(\chi)\sin\chi\sin^2\frac{\chi}{2}d\chi\rangle$, where v_r is the most probable speed of the buffer gas molecule, $\sigma(\chi)$ [50] is the differential collision cross section, $\chi_{\rm min} = \cos^{-1}(1-\frac{Um}{\mu^2v_r^2})$ is the minimum scattering angle corresponding to the escape of the initially trapped atom from the optical lattice, and $\mu = \frac{mM}{m+M}$ is the reduced mass. The braces indicate the averaging over all the possible speeds v_r of buffer gas molecules. Using the impulse approximation [50] one can obtain $\sigma(\chi) = \frac{1}{48}(\frac{15\pi C_6(m+M)\csc^7(\frac{\chi}{2})}{2mMv_r^2})^{\frac{1}{3}}$. The corresponding heating rate is $\frac{dT_{\rm Hg}}{dt} = \frac{\sqrt{\pi}n}{5\sqrt{2}mk_B}\Gamma(\frac{11}{6})(\frac{15\pi C_6k_BT}{M}(\sqrt{\frac{Um}{2}})^5)^{\frac{1}{3}}$. At the previously specified buffer gas parameters, the calculated collisional heating rate is $\frac{dT_{\rm Hg}}{dt} = 0.27$ μK/s. To calculate the heating and loss rates for Sr atoms we estimated the van der Waals coefficient as $C_{6,{\rm Sr}} = \frac{3}{2}\frac{I_{\rm Sr}I_{\rm bg}}{I_{\rm Sr}+I_{\rm bg}}\frac{\alpha_{\rm Sr}\alpha_{\rm bg}}{(4\pi\epsilon_0)^2}$, where $\alpha_{\rm Sr,bg}$ and $I_{\rm Sr,bg}$ are the polarizabilities and ionization potentials of the colliding Sr atom and buffer gas molecule. The ionization energy of molecular nitrogen is $I_{N_2} = 1503$ kJ mol^{-1}. The polarizability [54] $\alpha_{N_2} = 11.74$ a.u. The corresponding Sr loss rate at $U \sim 10$ ER,Sr $395 = 1.65$ μK is $\gamma_{\rm Sr,loss} = 0.7$ s^{-1}, $\frac{dT_{\rm Sr}}{dt} = 0.23$ μK/s. An additional laser field could be used to cool the atoms during the "dark periods" between the subsequent interrogations.

The rate of spontaneous photon scattering from the lattice field ($\lambda_L = 360$ nm) by Hg atoms trapped in the ground $^1S_0$ state is given by $\gamma_{\rm scat} \sim \frac{\Omega_{\rm Rabi}^2}{4\Delta^2}$ [55], where $\Omega_{\rm Rabi}$ is the Rabi frequency of the $^1S_0$-$^3P_1$ transition, and the detuning from the $^1S_0$-$^3P_1$ transition frequency $\Delta = \omega_{\rm res} - \omega_{\rm L}$. Considering the large detuning between the frequencies of the lattice field and the resonant frequency of the $^1S_0$-$^3P_1$ transition, such that $\Delta \gg \Omega_{\rm Rabi}$, the heating due to the spontaneous scattering can be neglected.

Another source of heating comes from the lattice intensity noise [56]. The corresponding heating rate is given by $\frac{dT_{\rm noise}}{dt} = \sum_N P_N(N+\frac{1}{2})\hbar\Omega_{\rm trap}\frac{\Omega^2_{\rm trap}}{4}S_\epsilon(2\nu_{\rm trap})$, where $S_\epsilon(2\nu_{\rm trap})$ is the fractional laser intensity noise power spectrum, evaluated at twice the trapping frequency $\nu_{\rm trap}$, N is the vibrational state of the trapped atom inside the lattice, and P_N is the population of the given vibrational state N. Using the polarizability values given in [57] the corresponding heating rate of Hg atoms in the ground vibrational state can be estimated as $\frac{dT^{\rm noise}_{\rm Hg}}{dt} = 534(\frac{I_0}{\rm kW/cm^2})^{\frac{3}{2}}S_\epsilon(2\times 13.1\sqrt{\frac{I_0}{\rm kW/cm^2}}\ {\rm kHz}){\rm K\,s^{-1}}$, where I_0 is the lattice field intensity. For the lattice potential depth $U \sim 10E_{\rm R,Hg} = 3.67\,\mu$K, the corresponding heating rate is $\frac{dT^{\rm noise}_{\rm Hg}}{dt} \approx 2.59\times 10^4 S_\epsilon(94\ {\rm kHz})\ {\rm K\,s^{-1}}$. As an example, we take the fractional intensity noise power spectrum of an argon ion laser [56] often used to pump the Ti:sapphire and dye lasers [58]. The resulting upper limit on the heating rate is $\frac{dT^{\rm noise}_{\rm Hg}}{dt} \approx 25.9\ {\rm nK\,s^{-1}}$. For Sr atoms the estimates are $\frac{dT^{\rm noise}_{\rm Sr}}{dt} = 3724(\frac{I_0}{\rm kW/cm^2})^{\frac{3}{2}}S_\epsilon(2\times 25.05\sqrt{\frac{I_0}{\rm kW/cm^2}}\ {\rm kHz})\,{\rm K\,s^{-1}}$. For the same fractional intensity noise spectrum and the potential depth $U \sim 10E_{\rm R,Sr} = 1.65\,\mu$K, one has $\frac{dT^{\rm noise}_{\rm Sr}}{dt} \approx 7.92\ {\rm nK\,s^{-1}}$.

The residual birefringence of the fiber causes the nonuniformity of the polarization along the lattice. This results in additional clock transition frequency uncertainty. The ^{87}Sr clock transition frequency shift due to the contribution of the vector and tensor polarizabilities was parametrized in [59] as $\Delta\nu_{v,t} = [0.22{\rm Hz}\,m_F\xi(\mathbf{e_k}\cdot\mathbf{e_B}) - 0.0577\,{\rm mHz}\,\beta]U/E_R$, where U is the lattice potential depth, E_R is the recoil energy, $\mathbf{e_k}$,$\mathbf{e_B}$ are the unitary vectors along the lattice wave vector and the quantization axis, $\beta = (3|\mathbf{e}\cdot\mathbf{e_B}|^2-1)[3m_F^2 - F(F+1)]$, $\mathbf{e}$ is the complex lattice laser polarization vector, and ξ is the degree of the ellipticity of the lattice field. Taking $(\mathbf{e_k}\cdot\mathbf{e_B}) = 1$, $\Delta\xi \sim \frac{\pi\Delta n}{\lambda_L}L \ll 1$, where Δn is the difference in the refractive indexes for two orthogonal polarizations and L is the length of the atomic cloud inside the fiber, one can estimate the vector polarizability induced frequency shift uncertainty as $\delta\nu_{v,m_F} \sim \frac{\pi}{\lambda_L}m_F\Delta nLU/E_R \times 0.22\ {\rm Hz}\,U/E_R$. For $m_F = 9/2$ and $\Delta n \sim 10^{-7}$ [21], $\delta\nu_{v\frac{9}{2}} = 3.1\ {\rm Hz}\frac{L}{\lambda}\frac{U}{E_R}\times 10^{-7}$. For $L = 8.13$ cm and $U = 10\ E_R$, $\delta\nu_{v\frac{9}{2}} = 0.3$ Hz. The vector light shifts of the components $m_F = \pm\frac{9}{2}$ have the opposite signs and can be eliminated. Indeed the Zeeman shift and vector light shift cancellation techniques have been developed in [60] based on the averaging of frequency measurements for two transitions $(^1S_0, F = \frac{9}{2}, m_F = \pm\frac{9}{2}) - (^3P_0, F = \frac{9}{2}, m_F = \pm\frac{9}{2})$. For the same parameters Δn, L, U, and $(\mathbf{e_k}\cdot\mathbf{e_B}) = 0$, $(\mathbf{e}\cdot\mathbf{e_B}) = 1$, $\delta\nu_{t\frac{9}{2}} = 41.5$ mHz. The dipole polarizabilities of ^{199}Hg at the magic wavelength $\lambda_L = 360$ nm are lower than the corresponding values for the Sr atom [57]. Therefore, the vector and tensor frequency shifts are not exceeding those for the ^{87}Sr atom. Although for bosonic isotopes there are neither tensor nor vector shifts, the polarization instability along the axis may lead to multipolar frequency shifts [61,62], which are, however, much weaker than those due to the electric-dipole interaction [57]. To mitigate such shifts, one could consider using the circularly polarized optical lattice for atomic clocks with bosonic isotopes.

IV. SUMMARY

We have studied the feasibility of an optical lattice clock based on the ultranarrow $^1S_0$-$^3P_0$ transition in Hg and other divalent atoms optically trapped inside the micron-scale hollow-core waveguide. The effect of the atom-surface interaction on the clock transition frequency inaccuracy at nonzero surface temperature has been evaluated. For an ensemble of cold atoms, with the temperature $T_a \sim \mu$K, optically trapped on the axis of a silica capillary (with surface temperature $T_S = 293$ K), the main contribution to the surface induced $^1S_0$-$^3P_0$ transition frequency shift comes from the nonresonant part of Casimir-Polder interaction potential. This contribution is substantially suppressed for Hg and Cd atoms compared to the other divalent atoms due to their relatively low differential static polarizability. For example, at the inner capillary radius $R_{\rm in} = 15\ \mu$m and the capillary thickness $d = 1\ \mu$m, the CP interaction induced $^1S_0$-$^3P_0$ transition frequency shift is $\delta\nu_{\rm Hg}/\nu_{\rm Hg} = 0.03\delta\nu_{\rm Sr}/\nu_{\rm Sr} = 0.27\times 10^{-18}$. For the silica capillary waveguide $\epsilon_r = 2.45$, the calculated upper limits on the $^1S_0$-$^3P_0$ transition frequency shift caused by the resonant atom-waveguide coupling effects are below 3×10^{-18}. In general, this shift and the natural linewidth broadening (Purcell effect) can be controlled by a proper choice of the geometric parameters of the waveguide. One could consider the possibility of compensating the nonresonant part of Casimir-Polder interaction on the core axis in combination with its resonant part at certain geometries of the waveguide. Additional effects may appear in the case of the resonances in dielectric constants of waveguide material.

We also estimated the atom loss and heating due to collisions with the buffer gas particles, lattice intensity noise induced heating, heating due to spontaneous photon scattering, and the residual birefringence induced frequency shifts. To fully realize the intriguing potential of the fiber clock, one needs to solve the problem of the residual buffer gas pressure limiting the interrogation time of the atomic ensemble and the number of atoms which can be loaded into the fiber before they escape the trapping potential.

ACKNOWLEDGMENTS

We thank K. Gibble and H. Katori for motivating discussions. We also thank V. Dzuba for the Cd data. This work was supported in part by the U.S. National Science Foundation through Grants No. PHY-1521560 and No. PHY-1607396.

[1] P. Treutlein, P. Hommelhoff, T. Steinmetz, T. W. Hänsch, and J. Reichel, Phys. Rev. Lett. **92**, 203005 (2004).

[2] F. Ramírez-Martínez, C. Lacroûte, P. Rosenbusch, F. Reinhard, C. Deutsch, T. Schneider, and J. Reichel, Adv. Space Res. **47**, 247 (2011).

[3] C. Deutsch, F. Ramirez-Martinez, C. Lacroûte, F. Reinhard, T. Schneider, J. N. Fuchs, F. Piéchon, F. Laloë, J. Reichel, and P. Rosenbusch, Phys. Rev. Lett. **105**, 020401 (2010).

[4] R. Gerritsma, S. Whitlock, T. Fernholz, H. Schlatter, J. A. Luigjes, J.-U. Thiele, J. B. Goedkoop, and R. J. C. Spreeuw, Phys. Rev. A **76**, 033408 (2007).

[5] W. Griffith, S. Knappe, and J. Kitching, Opt. Exp. **18**, 27167 (2010).

[6] L. M. Lust and D. W. Youngner, U.S. Patent 7,359,059 (2008).

[7] H. C. Abbink, E. Kanegsberg, and R. A. Patterson, U.S. Patent 7,239,135 (2007).

[8] E. J. Eklund, A. M. Shkel, S. Knappe, E. Donley, and J. Kitching, Sens. Actuators A **143**, 175 (2008).

[9] Y.-J. Wang, D. Z. Anderson, V. M. Bright, E. A. Cornell, Q. Diot, T. Kishimoto, M. Prentiss, R. A. Saravanan, S. R. Segal, and S. Wu, Phys. Rev. Lett. **94**, 090405 (2005).

[10] S. A. Schulz, Ph.D. thesis, University of Ulm, 2009.

[11] B. Fröhlich and Z. Yuan, Nat. Photon. **9**, 781 (2015).

[12] J. Cartwright, Quantum cryptography is safe again, Aug. 29, 2013, http://www.sciencemag.org/news/2013/08/quantum-cryptography-safe-again.

[13] R. B. Langley, GPS World **2**, 38 (Nov./Dec. 1991), available at http://www2.unb.ca/gge/Resources/gpsworld.nov-dec91.corr.pdf.

[14] J. Kitching, GPS World **18**, 52 (Nov. 2007), available at http://www2.unb.ca/gge/Resources/gpsworld.november07.pdf.

[15] T. Krawinkel and S. Schön, GPS World **27**, 50 (2016).

[16] T. A. Ely, D. Murphy, J. Seubert, J. Bell, and D. Kuang, in *24th AAS/AIAA Space Flight Mechanics Meeting, Spaceflight Mechanics 2014*, Advances in the Astronautical Sciences, Vol. 152, edited by R. S. Wilson, R. Zanetti, D. L. Mackison, and O. Abdelkhali (Univelt, San Diego, 2014), p. 51, available at https://www.researchgate.net/publication/260036335_Expected_Performance_of_the_Deep_Space_Atomic_Clock_Mission.

[17] S. Knappe, in *Comprehensive Microsystems*, edited by Y. B. Gianchandani, O. Tabata, and H. Zappe (Elsevier, Amsterdam, 2008), Vol. 3, p. 571.

[18] T. Kishimoto, H. Hachisu, J. Fujiki, K. Nagato, M. Yasuda, and H. Katori, Phys. Rev. Lett. **96**, 123001 (2006).

[19] J. Fortagh, A. Grossmann, C. Zimmermann, and T. W. Hänsch, Phys. Rev. Lett. **81**, 5310 (1998).

[20] R. F. Cregan, B. J. Mangan, J. C. Knight, T. A. Birks, P. S. J. Russell, P. J. Roberts, and D. C. Allan, Science **285**, 1537 (1999).

[21] S. Okaba, T. Takano, F. Benabid, T. Bradley, L. Vincetti, Z. Maizelis, V. Yampol'skii, F. Nori, and H. Katori, Nat. Comm. **5**, 4096 (2014).

[22] H. Katori, in *Proceedings of the 6th Symposium on Frequency Standards and Metrology*, edited by P. Gill (World Scientific, Singapore, 2002), p. 323.

[23] B. J. Bloom, T. L. Nicholson, J. R. Williams, S. L. Campbell, M. Bishof, X. Zhang, W. Zhang, S. L. Bromley, and J. Ye, Nature **506**, 71 (2014).

[24] I. Ushijima, M. Takamoto, M. Das, T. Ohkubo, and H. Katori, Nat. Photon. **9**, 185 (2015).

[25] A. Derevianko and M. Pospelov, Nat. Phys. **10**, 933 (2014).

[26] P. Wcisło, P. Morzyński, M. Bober, A. Cygan, D. Lisak, R. Ciuryło, and M. Zawada, Nat. Astron. **1**, 0009 (2016).

[27] M. Gross and S. Haroche, Phys. Rep. **93**, 301 (1982).

[28] D. Meiser, J. Ye, D. R. Carlson, and M. J. Holland, Phys. Rev. Lett. **102**, 163601 (2009).

[29] D. Yu and J. Chen, Phys. Rev. Lett. **98**, 050801 (2007).

[30] H. Hachisu, K. Miyagishi, S. G. Porsev, A. Derevianko, V. D. Ovsiannikov, V. G. Pal'chikov, M. Takamoto, and H. Katori, Phys. Rev. Lett. **100**, 053001 (2008).

[31] M. Petersen, R. Chicireanu, S. T. Dawkins, D. V. Magalhães, C. Mandache, Y. Le Coq, A. Clairon, and S. Bize, Phys. Rev. Lett. **101**, 183004 (2008).

[32] J. J. McFerran, L. Yi, S. Mejri, S. Di Manno, W. Zhang, J. Guéna, Y. Le Coq, and S. Bize, Phys. Rev. Lett. **108**, 183004 (2012); **115**, 219901(E) (2015).

[33] M. Takamoto, I. Ushijima, M. Das, N. Nemitz, T. Ohkubo, K. Yamanaka, N. Ohmae, T. Takano, T. Akatsuka, A. Yamaguchi, and H. Katori, C.R. Phys. **16**, 489 (2015).

[34] R. Tyumenev, M. Favier, S. Bilicki, E. Bookjans, R. Le Targat, J. Lodewyck, D. Nicolodi, Y. Le Coq, M. Abgrall, J. Guéna, L. De Sarlo, and S. Bize, New J. Phys. **18**, 113002 (2016).

[35] S. G. Porsev and A. Derevianko, Phys. Rev. A **74**, 020502 (2006).

[36] S. Fevrier, F. Gerome, A. Labruyere, B. Beaudou, J. Humbet, and J.-L. Auguste, Opt. Lett. **34**, 2888 (2009).

[37] F. Gebert, M. H. Frosz, T. Weiss, Y. Wan, A. Ermolov, N. Y. Joly, P. O. Schmidt, and P. St. J. Russell, Opt. Express **22**, 15388 (2014).

[38] A. Derevianko, B. Obreshkov, and V. A. Dzuba, Phys. Rev. Lett. **103**, 133201 (2009).

[39] S. Å. Ellingsen, S. Y. Buhmann, and S. Scheel, Phys. Rev. A **82**, 032516 (2010).

[40] W. Jhe, A. Anderson, E. A. Hinds, D. Meschede, L. Moi, and S. Haroche, Phys. Rev. Lett. **58**, 666 (1987).

[41] M. Gorza and M. Ducloy, Eur. Phys. J. D **40**, 343 (2006).

[42] J. M. Wylie and J. E. Sipe, Phys. Rev. A **30**, 1185 (1984).

[43] J. M. Wylie and J. E. Sipe, Phys. Rev. A **32**, 2030 (1985).

[44] L. W. Li, M.-S. Leong, T.-S. Yeo, and P.-S. Kooi, J. Electromagn. Waves Appl. **14**, 961 (2000).

[45] D. Grass, J. Fesel, S. G. Hofer, N. Kiesel, and M. Aspelmeyer, Appl. Phys. Lett. **108**, 221103 (2016).

[46] A. Derevianko, S. Porsev, and J. Babb, At. Data Nucl. Data Tables **96**, 323 (2010).

[47] V. A. Dzuba (private communication).

[48] H. B. G. Casimir and D. Polder, Phys. Rev. **73**, 360 (1948).

[49] A. Afanasiev and V. Minogin, Phys. Rev. A **82**, 052903 (2010).

[50] R. E. Johnson, *Atomic and Molecular Collisions*, Vol. 2 (Academic, New York, 1987).

[51] M. Bajcsy, S. Hofferberth, T. Peyronel, V. Balic, Q. Liang, A. S. Zibrov, V. Vuletic, and M. D. Lukin, Phys. Rev. A **83**, 063830 (2011).

[52] H. Margenau, Phys. Rev. **40**, 387 (1932).

[53] S. Atutov, N. Danilina, S. L. Mikerin, and A. Plekhanov, Opt. Comm. **315**, 362 (2014).

[54] D. Spelsberg and W. Meyer, J. Chem. Phys. **111**, 9618 (1999).

[55] J. D. Miller, R. A. Cline, and D. J. Heinzen, Phys. Rev. A **47**, R4567 (1993).

[56] T. A. Savard, K. M. O'Hara, and J. E. Thomas, Phys. Rev. A **56**, R1095 (1997).

[57] H. Katori, V. D. Ovsiannikov, S. I. Marmo, and V. G. Palchikov, Phys. Rev. A **91**, 052503 (2015).

[58] R. P. Scott, C. Langrock, and B. H. Kolner, IEEE J. Sel. Top. Quant. Electron. **7**, 641 (2001).

[59] P. G. Westergaard, J. Lodewyck, L. Lorini, A. Lecallier, E. A. Burt, M. Zawada, J. Millo, and P. Lemonde, Phys. Rev. Lett. **106**, 210801 (2011).

[60] M. Takamoto, F.-L. Hong, R. Higashi, Y. Fujii, M. Imae, and H. Katori, J. Phys. Soc. Jpn. **75**, 104302 (2006).

[61] A. V. Taichenachev, V. I. Yudin, V. D. Ovsiannikov, V. G. Pal'chikov, and C. W. Oates, Phys. Rev. Lett. **101**, 193601 (2008).

[62] H. Katori, K. Hashiguchi, E. Y. Il'inova, and V. D. Ovsiannikov, Phys. Rev. Lett **103**, 153004 (2009).